



Bi-metallic MOFs possessing hierarchical synergistic effects as high performance electrocatalysts for overall water splitting at high current densities

Hao-Wei Lin, Duraisamy Senthil Raja, Xui-Fang Chuah, Cheng-Ting Hsieh, Yu-An Chen, Shih-Yuan Lu*

Department of Chemical Engineering, National Tsing Hua University, Hsinchu 30013, Taiwan

ARTICLE INFO

Keywords:

Metal-organic framework (MOF)
Alkaline water electrolysis
Bimetallic MOF
Hydrogen evolution reaction
Oxygen evolution reaction

ABSTRACT

Bi-metallic metal organic framework (MOF) compounds, FeNi(BDC)(DMF,F), adequately modulated through alloying of Ni and Fe, were demonstrated outstanding electrocatalysts for overall water splitting. It was composed of two well mixed bi-metallic MOF phases, Fe-rich FeNi(BDC)(DMF,F) and Ni-rich FeNi(BDC)(F), each containing two molecularly well mixed metallic clusters, to give pronounced hierarchical synergistic effects toward overall water splitting, delivering current densities of 10 and 400 mA cm⁻² at ultralow cell voltages of 1.58 and 1.90 V, respectively, outperforming the pairing of benchmark electrodes, Pt-C//IrO₂. The stability of the electrodes was also excellent, experiencing only minor chronoamperometric decay after a continuous operation at 400 mA cm⁻² for 30 h. The success may be attributed to the MOF/substrate synergistic effects between the FeNi(BDC)(DMF,F) and the conductive macroporous nickel foam, the inter-molecular synergistic effects between the two constituent MOF phases, and the intra-molecular synergistic effects between the FeO₆ and NiO₆ clusters of the Fe-rich FeNi(BDC)(DMF,F).

1. Introduction

Energy storage is an indispensable part of the green energy infrastructure. It is particularly critical to tackle the detrimental issues of unreliability and intermittency associated with renewable energies [1,2]. Among the many approaches developed/under development, hydrogen production from renewable energy driven electrolytic water splitting, storing excessive off-peak electricity generated by renewable energies in the form of chemical energy, has drawn a great deal of resurging research attention in recent years [3,4]. Because of its high gravimetric energy density (140.4 MJ/kg) and zero carbon emission during utilization, hydrogen is undoubtedly an excellent energy carrier for energy storage. In fact, the renewable energy driven electrolytic water splitting technology, the so-called power-to-gas (P2G) technology, combining subsequent gas-to-power (G2P) technologies such as hydrogen fuel cell systems [5,6], can indeed offer a reliable solution to utilization of renewable energies.

A typical electrolytic water splitting process consists of two half-cells: cathode for the hydrogen evolution reaction (HER) and anode for the oxygen evolution reaction (OER). Here, the OER, a four electron transfer reaction, is kinetically more complex and sluggish than HER, a

two electron transfer reaction, and thus requires higher overpotentials [7]. Attempts have been made to replace water with organic chemicals such as hydroxymethylfurfural (HMF) to avoid the OER at the anode [8]. The high cost and limited availability of the organic compounds however restricts further development of this practice for large-scale applications.

IrO₂ and Pt/C, popular benchmark electrocatalysts for the OER and HER, respectively, offer low overpotentials to drive the water splitting [9,10]. Nevertheless, these noble metal based electrocatalysts suffer from the high cost, Earth-scarcity, and unsatisfactory long-term stability under high current densities. As a result, it is critical to develop high efficiency non-noble metal based, cost-effective, and durable electrocatalysts. A wide variety of metal oxides [11,12], phosphides [13–18], hydroxides [19,20], hydrosilicates [21], and even chalcogenides [22–26] has been developed to achieve low working cell voltages to save the electricity cost that accounts for more than 50% of the operation cost of electrolytic water splitting. Nevertheless, most of the reported electrodes were evaluated in terms of overpotentials and stability at low current densities, which are not practical for large-scale applications. In view of this, we have recently developed several electrocatalysts, including mixed NiO/NiCo₂O₄ nanocrystals on nickel foam

* Corresponding author.

E-mail addresses: sylu@mx.nthu.edu.tw, sylu@che.nthu.edu.tw (S.-Y. Lu).

<https://doi.org/10.1016/j.apcatb.2019.118023>

Received 25 April 2019; Received in revised form 13 July 2019; Accepted 27 July 2019

Available online 01 August 2019

0926-3373/ © 2019 Elsevier B.V. All rights reserved.

(NF) [27], N-doped C/Ni₅P₄/Fe₃P hollow nanocubes [28], N-doped graphene layer coated Fe-Ni alloy nanoparticles encapsulated within an N-doped carbon hollow nanobox [29], well mixed Ni-Fe oxides on Ni foam [30], NiFe/(Ni,Fe)₃S₂ core/shell nanowire arrays [31], and NiFe alloy nanotube arrays [32] as efficient and durable electrocatalysts for the OER at high current densities.

Metal organic frameworks (MOFs), possessing versatile catalytic activities, remarkable structural diversity, high surface areas, and tunable pore sizes, have been applied to a wide range of applications including chemical sensing [33,34], supercapacitor [35,36], and gas storage [37] in recent years. MOFs are basically composed of metal clusters coordinated with organic linkers and solvent molecules [38,39]. During a specific catalytic reaction, the labile coordinated solvent molecules tend to dissociate, resulting in formation of coordinatively unsaturated metal centers (CUMCs) in the MOF structure [40]. Depending on coordinated metal components, the CUMCs may act as typical Lewis acid centers to exhibit versatile catalytic activities. Nevertheless, because of their low electrical conductivities (about 10^{-10} S m⁻¹) [41], only very few MOFs have been directly used as efficient electrocatalysts for the OER and HER. More often, they are utilized as the precursors to derive carbonaceous materials carrying metal or metal-based electrocatalysts through high temperature thermal treatments [42,43]. There are however potential drawbacks associated with this practice, including collapse of advantageous nanostructure, agglomeration of metal centers, and loss of active sites during the high temperature treatment, leading to decrease in achievable current densities and deteriorated long-term stability [44].

An effective way to improve on the low electrical conductivity situation is to load catalytic MOFs on conductive substrates. Duan et al. demonstrated this approach with an in-situ growth of a MOF nanosheet array on a conductive substrate through a dissolution-crystallization process [44]. Raja et al. developed a water-stable MOF, NH₂-MIL-88B (Fe₂Ni) [42], and also well mixed Fe- and Ni-MOFs [45] in-situ grown on nickel foam to form MOF/NF composite electrodes, that exhibited outstanding electrocatalytic performances toward the OER and HER along with excellent stability at high current densities. When utilized as electrocatalysts, MOFs show distinct catalytic properties as compared with traditional metal-based ones, such as alloys, metal oxides, metal sulfides, and metal phosphides. For instance, the optimal metallic composition of Fe and Ni found in bimetallic NiFe MOFs for achieving best electrochemical performances [46] is different from that reported in literature for NiFe alloys [47]. Furthermore, MOF based electrocatalysts may offer more possibilities to induce synergistic effects to boost catalytic performances. Synergistic effects between MOF and hosting conductive substrates were identified as one of the main contributors to the success of MOF based composite electrocatalysts [34]. In fact, synergistic effects can be explored much more in depth to significantly further boost the electrocatalytic performances of the MOF material toward the OER and HER. In addition to the MOF/substrate synergistic effect, synergistic effects functioning at even smaller length scales can be designed, e.g., inter-molecular synergistic effects between two well mixed functioning MOFs and intra-molecular synergistic effects between different metal clusters of a multi-metallic MOF. With the above considerations combined, a new concept of hierarchical synergistic effects is proposed and realized in this work. The realization of the hierarchical synergistic effects is achieved through adequately alloying the metallic components of a bi-metallic MOF, which is grown in-situ on the skeleton surfaces of a porous conductive substrate. The modulation of the molar ratio of the two metallic components of the bi-metallic MOF, leads to formation of two well mixed phases of the MOFs with each MOF phase containing two molecularly well mixed metallic clusters. With such material design, one can create three levels of synergistic effects, including the MOF/substrate, inter-molecular, and intra-molecular ones, realizing the hierarchical synergistic effect concept.

With a facile one-step solvothermal process, FeNi(BDC)(DMF,F) can

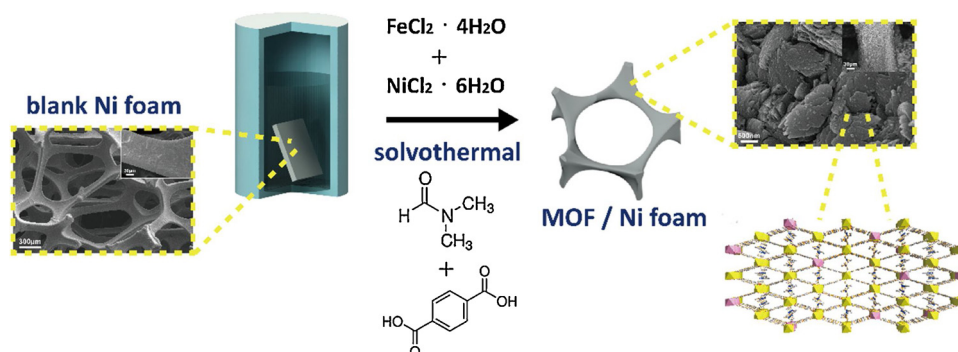
be firmly grown in-situ on the skeleton surfaces of nickel foam to form a binder-free FeNi(BDC)(DMF,F)/NF electrode. Traditionally, electrocatalysts are prepared in powdery form [13,48], and binders are required to load the catalysts onto the substrate to form the electrode. Most binders are however non-conductive polymeric materials, such as polyvinylidene difluoride, and the presence of the non-conductive binder would decrease the exposure of the active sites of the catalyst to the electrolyte and reduce the overall electrical conductivity of the electrode [49]. Furthermore, the adhesion between the binder and the catalyst powders may not be strong enough to resist the large shear stresses generated from the violent generation and release of oxygen and hydrogen bubbles when operated at high current densities, and catalyst detachment from the electrode would deteriorate the long term stability of the electrode [50,51]. In-situ growth of the electrocatalyst on the skeleton surfaces of the conductive substrate offers firm close contact between the substrate and the catalyst to not only enhance the charge transport across the catalyst/substrate interface but also improve the mechanical integrity of the electrode for better stability. This can be proved by comparing the electrocatalytic performances of the FeNi(BDC)(DMF,F)/NF electrode with those achieved by the electrode formed through coating bulk FeNi(BDC)(DMF,F) powders onto NF with binders. Furthermore, with a suitable molar ratio of the Fe and Ni precursors, two well mixed phases of FeNi(BDC)(DMF,F), one Fe-rich FeNi(BDC)(DMF,F) and the other Ni-rich FeNi(BDC)(F), were formed to offer inter-molecular synergistic effects, with the FeO₆ and NiO₆ clusters contained in each phase providing intra-molecular synergistic effects.

In this study, the adequately modulated FeNi(BDC)(DMF,F)/NF electrode delivered current densities of 60 and 400 mA cm⁻² at ultralow overpotentials of 227 and 252 mV, respectively toward the OER, with an ultralow Tafel slope of 37.4 mV dec⁻¹ achieved. Moreover, if serving as a bifunctional electrode, it required only 1.58 and 1.90 V to achieve the current densities of 10 and 400 mA cm⁻², respectively for overall water splitting, which is even superior to the pairing of the two benchmark electrodes, Pt-C/NF//IrO₂/NF. For the stability test, with the help of the nickel foam substrate that can withstand high mechanical stresses and allow fast mass transport of reactants and products such as hydrogen and oxygen through its macroporous channels [52], the FeNi(BDC)(DMF,F)/NF electrode showed excellent durability under operation at a high current density of 400 mA cm⁻², making it suitable for large scale applications. The concept of hierarchical synergistic effects can be readily extended to other bi-metallic and even multi-metallic MOF systems for a wide range of electrochemical applications.

2. Experimental section

2.1. Chemicals and characterizations

All chemicals and reagents were of analytical grade and used without further purification. Commercial NF (thickness: 1.8 mm) was purchased from Changsha Liyuan Port (Changsha, China) and cut into pieces of 2.5 cm × 2.5 cm, which were further down-sized to 1 cm × 2.5 cm after solvothermal treatment for in-situ growth of MOF. To remove the thin oxide layer present on the skeleton surface of NF, NF was ultrasonicated in 3 M HCl for 30 min, followed by washing with water, ethanol, and acetone and drying in a vacuum oven set at 50 °C. The morphology of the electrodes was characterized with a field emission scanning electron microscope (FESEM) (Hitachi S-4800, Japan). EDX (Oxford 6857, Oxford Instruments) spectroscopy was conducted to determine the elemental composition and atomic ratio of Fe vs. Ni of the bulk MOF with an accelerating voltage of 15 kV. The crystalline structure of the MOF sample was examined with a powder X-ray diffractometer (Shimadzu XRD-6000, Japan) equipped with a 3 kW Cu X-ray tube. Fourier transform infrared (FT-IR) spectra were recorded on a Perkinelmer spectrometer (Spectrum Two) with the KBr pellet



Scheme 1. Schematic illustration of synthetic process for one-step in-situ growth of FeNi(BDC)(DMF,F) on nickel foam. Scale bar for SEM image of blank nickel foam is 300 μm (30 μm for inset image), and scale bar for SEM image of MOF on nickel foam is 500 nm (30 μm for inset image).

technique. XPS measurements were conducted to study the chemical state of the elements with a monochromatized Al K α X-ray as the excitation source (XPS, Thermo ESCALAB 250XI, USA).

2.2. Fabrication of electrode

With a one-step solvothermal method (Scheme 1), the MOF was grown on the skeleton surface of NF following the procedures reported in literature for the synthesis of FeNi(BDC)(DMF,F) [53] and Fe(BDC)(DMF) [54] with modifications. Briefly, benzene-1,4-dicarboxylic acid (BDC, 4 mmol) and mixture of FeCl₂·4H₂O and NiCl₂·6H₂O (4 mmol) mixed at different molar ratios were separately dissolved in 20 mL *N,N*-dimethylformamide (DMF) under stirring for 10 min. The two solutions were transferred into a 100 mL Teflon-lined autoclave with 1 pre-treated NF (2.5 cm \times 2.5 cm in size) placed inside. An amount of 0.8 mL HF (5 M) was then added into the autoclave under ultrasonic agitation for 15–20 minutes. The solvothermal proceeded at 150 $^{\circ}\text{C}$ for 72 h and was let cool to room temperature. The MOF loaded NF and the MOF powders collected at the bottom of the autoclave reactor was washed with DMF, DI water, and ethanol sequentially. The MOF/NF and MOF powders were dried at 70 $^{\circ}\text{C}$ overnight to afford the product electrode and bulk MOF.

Bulk MOF powders were casted on graphite electrodes (1 cm \times 1 cm) to serve as the bulk MOF electrode. An amount of 8.8235 mg of binder, polyvinylidene fluoride, was dissolved in 3 mL of organic solvent, *N*-methyl-2-pyrrolidinone, under ultrasonic agitation. Then, 1 mg of bulk MOF powders was dispersed in 60 μL of the above solution under ultrasonic agitation for 15 min to form a uniform suspension. Finally, 30 μL of the suspension was drop cast onto the surface of a graphite electrode uniformly and dried at 60 $^{\circ}\text{C}$ to afford the bulk MOF electrode with a catalyst loading of 0.5 mg cm⁻².

For the fabrication of bulk MOF/NF, Pt-C/NF, and IrO₂/NF electrodes, an amount of 2 mg catalyst powders (bulk MOF, Pt-C, or IrO₂) was dispersed in 280 μL of 50% aqueous ethanol and 120 μL of polyvinylidene fluoride (0.3 wt% in *N*-methylpyrrolidone as binder) under ultrasonic agitation for 30 min to form an ink-like suspension. An amount of 100 μL of the ink-like suspension was drop cast onto NF, followed by drying at 60 $^{\circ}\text{C}$, to afford the electrode with a catalyst mass loading of 0.5 mg cm⁻².

2.3. Electrochemical measurements

The electrocatalytic performances of the fabricated electrodes towards OER and HER were investigated on a CHI6275D electrochemical workstation with a three-electrode system in 1 M aqueous KOH solution. The fabricated electrode was used as the working electrode (1 cm \times 1 cm), with a platinum plate (1 cm \times 1 cm, for OER measurements) or a graphite plate (1 cm \times 1 cm, for HER measurements) as the counter electrode and Hg/HgO electrode as the reference electrode. To

obtain stable and reproducible current densities, the working electrode was conditioned with 30 cycles of cyclic voltammetry at a scan rate of 100 mV s⁻¹ before the linear sweep voltammetric (LSV) measurements for the OER and HER. After the conditioning, all the LSV polarization curves of the electrodes were recorded at a scan rate of 5 mV s⁻¹ to minimize the capacitive current effect. All potentials measured in this study were converted into voltage versus reversible hydrogen electrode (RHE) with the following Nernst equation: $E_{\text{RHE}} = E_{\text{Hg/HgO}} + 0.118 + 0.059 \times \text{pH}$. For the calculation, the overpotential (η) was acquired using the equation: $\eta = E_{\text{RHE}} - 1.23$ for the OER. All current densities reported were *iR*-compensated during the measurement. Electrochemical impedance spectroscopy (EIS) was conducted over a frequency range from 100 kHz to 100 mHz, taking the fabricated electrode as the working electrode. The applied alternating current voltage amplitude is 10 mV. The resulting Nyquist plot was fitted with a suitable equivalent circuit model to extract the critical data for the charge transfer resistance.

3. Results and discussion

The bi-metallic FeNi MOFs were prepared with a solvothermal method [53,54]. The metallic composition of the products was modulated, through varying the relative concentrations of the two metallic precursors, to investigate the optimal alloying extent of the metallic components of the bi-metallic MOF for achieving the best electrochemical performances in electrolytic water splitting. The relative molar concentrations of the two precursors investigated, FeCl₂·4H₂O and NiCl₂·6H₂O, are summarized in Table S1. The MOFs were grown in-situ on the skeleton surfaces of nickel foam as the working electrode, taking advantages of nickel foam as a porous conductive support for uniform dispersion of the MOF for full utilization of its electrocatalytic functions. Furthermore, for comparison purposes, the MOF products not deposited on nickel foam, termed bulk MOFs, were also collected for characterizations.

As shown in Fig. S1 (Supporting Information), the MOF loaded nickel foam electrodes, MOF/NF, prepared at different molar ratios of Fe and Ni precursors, exhibit distinct colors, from deep brown of Fe-only MOF/NF (Fe:Ni = 1:0) to dark silver of Ni-only MOF/NF (Fe:Ni = 0:1), implying significant differences in composition and even morphology of the product MOFs on NF. Fig. 1 shows the SEM images of the MOF/NF electrodes at increasing Ni precursor loading (0 to 100%), with blank NF (Fig. 1i) included for comparison. The insets show the morphologies of the corresponding NF skeletons. It is evident that the MOFs were uniformly grown on the skeleton surfaces of nickel foam with full coverage. As for the detailed morphology of the in-situ grown MOFs, it changes with increasing Ni precursor loading from the stacked thin slab structure of the Fe-only MOF (Fig. 1a) to nanorod array structure of the Ni-only MOF (Fig. 1h). The thin slabs shrink in size and thickness with increasing Ni precursor loading up to sample of

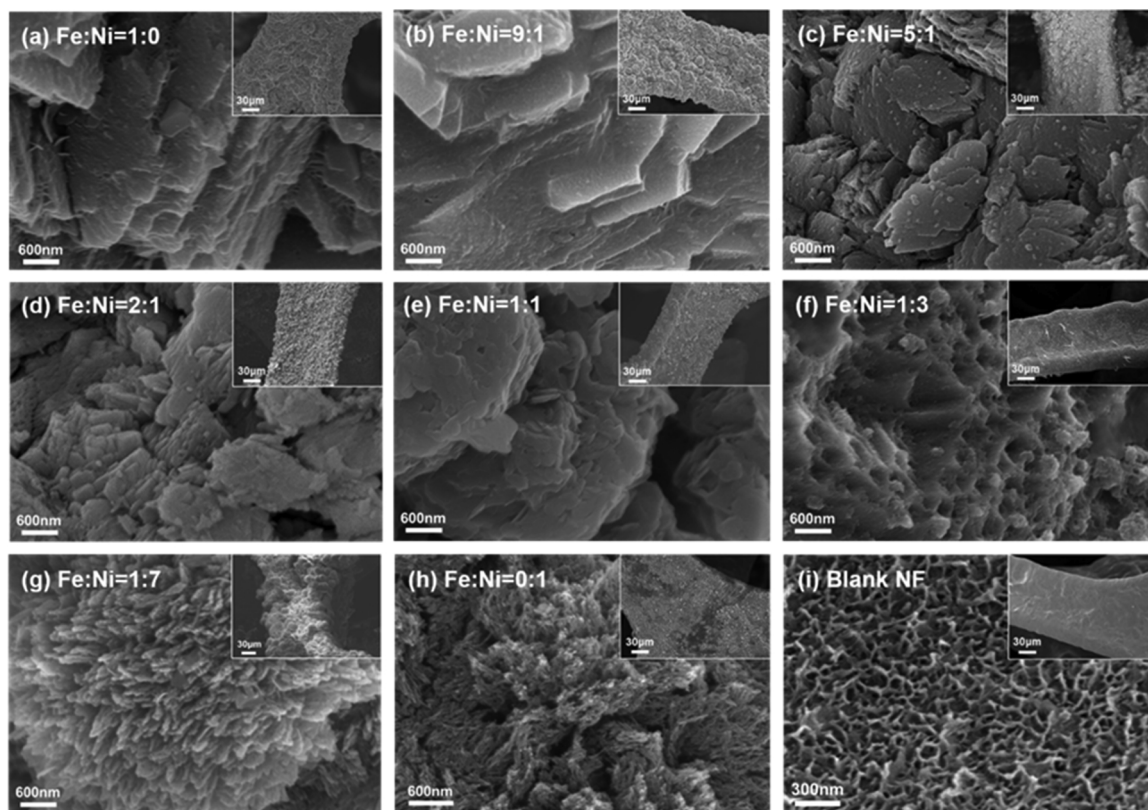


Fig. 1. SEM images of MOF/NF for precursor Fe:Ni ratios of (a) 1:0, (b) 9:1, (c) 5:1, (d) 2:1, (e) 1:1, (f) 1:3, (g) 1:7, and (h) 0:1, and (i) blank NF. Insets show SEM images of corresponding MOF coated skeletons of NF.

Fe:Ni of 2:1 (Fig. 1d). The morphology of sample of Fe:Ni of 1:1 (Fig. 1e) shifts from thin slab to irregular shape. If further increasing the Ni precursor loading, the morphology first turns into porous for sample of Fe:Ni of 1:3 (Fig. 1f), then to nanorod array for samples of Fe:Ni of 1:7 and 0:1 (Fig. 1g and h, respectively).

The compositions of the metallic components, i.e., atomic ratios of Fe/Ni, of the product bulk MOFs were estimated with EDX analyses, and the results are summarized in Table S2 for comparison. The Fe/Ni ratios of the precursors match with those of the corresponding products very well, considering the semi-quantitative nature of the EDX analysis. The Ni loading in the product increases with increasing Ni loading in the precursor as expected. Here, to confirm the EDX result, sample of Fe:Ni of 5:1, the best performing sample as discussed in latter sections, was further examined with XPS to determine the atomic ratio of Fe/Ni in the product bulk MOF. The result is summarized in Table S3. It shows a similar atomic ratio of Fe/Ni with that estimated from the EDX analysis, 4.2 vs. 4.5. Furthermore, EDX elemental mapping of the MOF/NF electrode fabricated with Fe:Ni of 5:1 (Fig. S2, Supporting Information) suggests the uniform distributions of the constituent elements in the product, including C, N, O, F, Fe, and Ni. Here, C is from the organic linker, BDC, N from the coordinated solvent molecule, DMF, O from both the organic linker and coordinated solvent, F from the coordinated additive, HF, and Fe and Ni from the two metallic precursors.

The crystalline structure of the product bulk MOFs was characterized with XRD. Fig. 2a and b show the XRD patterns of the product MOFs at increasing Ni precursor loading. Simulated XRD patterns of two relevant MOFs, Fe(BDC)(DMF) and Ni(BDC) [53,55], are also included for comparison. The two MOFs serve as the references for the Fe-only MOF and Ni-only MOF prepared in this work. It is evident that the XRD patterns of the Fe-only MOF and Ni-only MOF match well with the simulated ones of Fe(BDC)(DMF) and Ni(BDC), respectively. With increasing Ni loading in the product MOF, the XRD pattern shifts from that of the Fe-only MOF to that of the Ni-only MOF. For MOF products

of low Ni loading, there can be observed a clear peak splitting at around 9° , from which two constituent peaks of 8.97° and 9.10° can be identified. In addition, a new peak located at around 14.1° emerges with increasing Ni loading. The peak of 9.10° is contributed by an Fe-rich bimetallic FeNi-MOF, possessing similar crystalline structure with that of Fe(BDC)(DMF), whereas the peaks of 8.97° and 14.1° come from a Ni-rich bimetallic FeNi-MOF, possessing similar crystalline structure with that of Ni(BDC). The peaks of 9.10° and 11.0° , the two most pronounced diffraction peaks of the Fe-rich MOF, diminishes in intensity, whereas the peaks of 8.97° and 14° become more pronounced with increasing Ni loading. At the precursor Ni loading of 50% (Fe:Ni = 1:1), the two major diffraction peaks of the Fe-rich MOF almost disappear, with only the major diffraction peak located at 8.97° of the Ni-rich MOF remains. One can conclude from the above observations that there exist two MOF phases, one Fe-rich and the other Ni-rich. These two MOF phases are well mixed so that no phase separation, i.e., no distinct phase domains, can be observed in the SEM images of the product MOFs, as shown in Fig. 1. In terms of synergistic effects between two different phases, the well mixed state is advantageous since it implies close and large area contact of the two phases. In addition to bulk MOFs, the MOFs in-situ grown on the skeleton surface of nickel foam was also detached from nickel foam with ultrasonic agitation and collected for XRD characterizations. This type of MOF products is termed scratched-off MOFs. Fig. 2c shows the XRD pattern comparison between bulk and scratched-off MOFs of Fe:Ni of 5:1. The good agreement of the two XRD patterns confirms the same crystalline composition for the bulk and in-situ grown MOFs.

More structural information of the product MOFs was acquired with Fourier transform infrared spectroscopy (FTIR). The left panel of Fig. S4 (Supporting Information) shows the FTIR spectra recorded for all bulk MOFs of increasing Ni loading. If examined closely, with increasing Ni loading, the intensity of the absorption peak located at around 1685 cm^{-1} , which is attributable to the C–O stretching of DMF

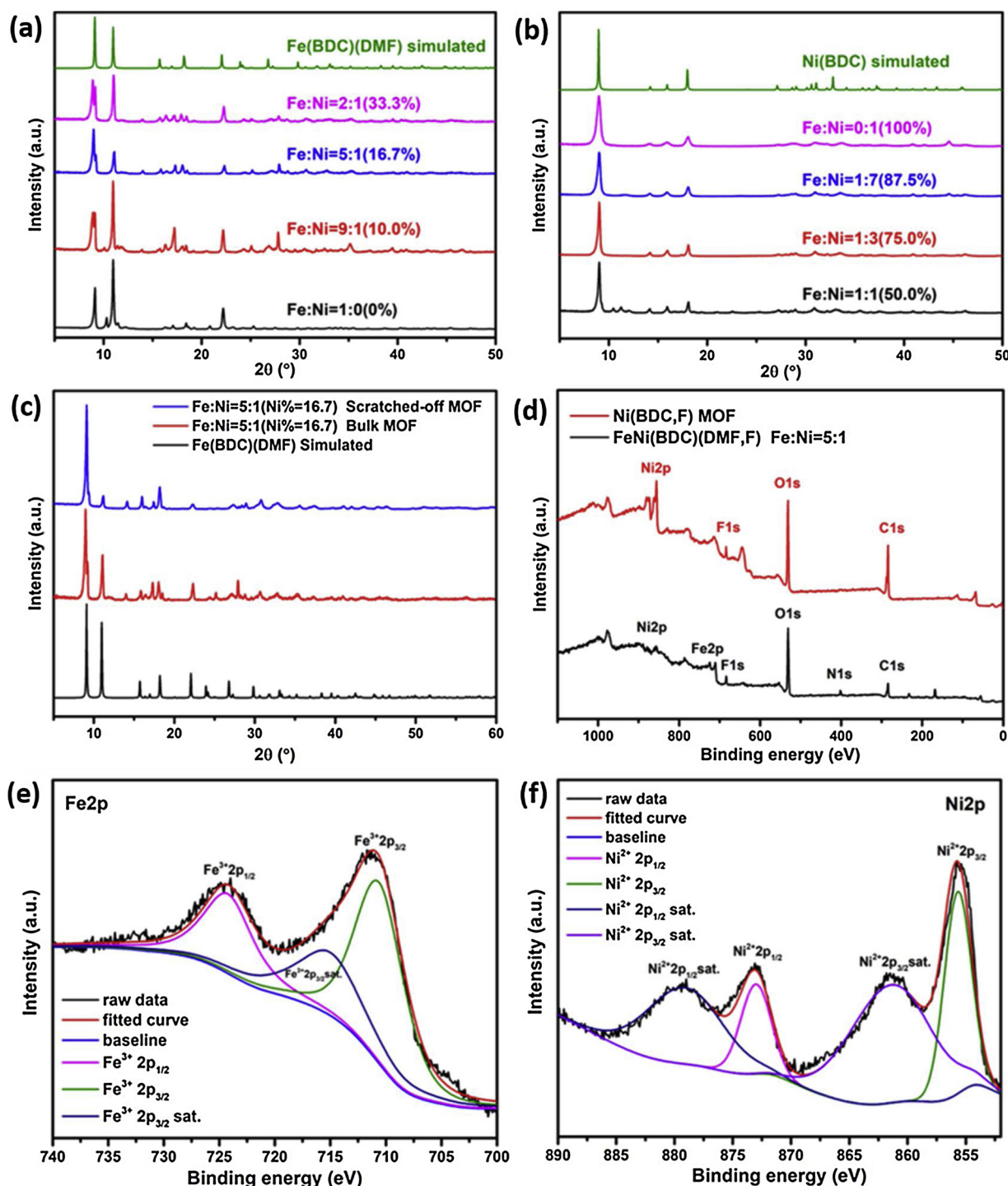


Fig. 2. Powder XRD patterns of bulk MOFs of precursor Ni% of (a) 0–33.3 and (b) 50–100. (c) XRD patterns of bulk and scratched-off MOFs of precursor Ni% of 16.7. (d) Full survey XPS spectra of bulk Fe-rich MOF of precursor Ni% of 16.7 and Ni-only MOF. High resolution XPS spectra of Fe-rich MOF/NF of precursor Ni% of 16.7: (e) Fe2p and (f) Ni2p.

molecules [56–58], decreases gradually and eventually disappears for samples of Fe:Ni of 1:7 and 0:1. This phenomenon implies that DMF molecules are coordinated to the core metal ions of the Fe-only and Fe-rich MOFs, but absent from the Ni-only and Ni-rich MOFs. This transition trend in the peak intensity of 1685 cm^{-1} in fact is in good consistency with the transition trends observed in morphology and XRD pattern at increasing Ni loading. With increasing Ni loading, the amount of the Fe-rich MOF in the two phase product decreases, whereas that of the Ni-rich MOF increases. The right panel of Fig. S4 (Supporting Information) shows the detailed FTIR spectrum of bulk MOF of Fe:Ni of

5:1. The absorption peaks of 1576 , 1380 , and 1018 cm^{-1} are attributed to the stretching vibrations of the carboxylate groups, whereas the peak at 749 cm^{-1} results from the bending vibrations of the C–H bond of benzene [53,54,59]. The two strong peaks located at 1576 and 1380 cm^{-1} are contributed by the asymmetric and symmetric stretching vibrations of the carboxyl groups, respectively, again confirming existence of the dicarboxylate linker [54,59]. Furthermore, the absorption bands at 541 and 445 cm^{-1} can be attributed to the characteristic stretching vibrations of the Fe–O and Ni–O bonds, respectively. If examined closely, the left panel of Fig. S4 shows the transition

trend in the peak intensities of the Fe–O and Ni–O bonds with increasing Ni loading, decreasing for the Fe–O signals and increasing for the Ni–O signals [60–62]. Furthermore, the absence of the characteristic band associated with the bridging hydroxyl group (Fe–O(H)–Fe), located at around 850 cm^{-1} , further confirms that it is DMF instead of hydrogen coordinated to the axial oxygen atom of the metal-oxygen cluster [60,63].

Fig. S5 (Supporting Information) shows the molecular structure of the reference Fe(BDC)(DMF) MOF. It is mainly composed of the trans corner-sharing octahedral chains, the bridging ligand benzene-1,4-dicarboxylic acid, and coordinated DMF molecules (Figs. S5a and S5b). The central Fe atom, along with the six surrounding oxygen atoms, forms the octahedral metal cluster MO_6 , linked together with the axial oxygen atoms provided by DMF through a trans corner-sharing pattern. The metal clusters MO_6 ($\text{M} = \text{Fe}, \text{Ni}$) are the active sites of the MOF catalysts and the organic linker plays a minor supporting role, not directly involved in the catalyzation process.

X-ray photoelectron spectroscopy (XPS) was conducted for bulk MOFs and MOF/NF to investigate their elemental chemical states and compositions. Fig. 2d shows the full survey XPS spectra of the Fe-rich MOF of Fe:Ni of 5:1 and Ni-only MOF, revealing the existence of common elements of C, O, and F. As expected, both Fe and Ni are detected for the Fe-rich MOF, whereas only Ni is present in the Ni-only MOF. Besides, the peaks around 645 and 713 eV are the Auger peaks of Ni. Also important to note is the absence of N from the spectrum of the Ni-only MOF, implying the absence of DMF coordination, whereas the presence of N in the spectrum of the Fe-rich MOF again confirms DMF coordination in the Fe-rich MOF as revealed in the FTIR analysis. As suggested by the XRD analysis, the Fe-rich bimetallic FeNi-MOF possesses a similar crystalline structure as that of the reference Fe(BDC)(DMF) MOF. Furthermore, with the presence of DMF and F confirmed with the XPS measurements, the Fe-rich bimetallic FeNi-MOF can be denoted more specifically as Fe-rich FeNi(BDC)(DMF,F). As for the Ni-rich bimetallic FeNi-MOF, it can be denoted more specifically as Ni-rich FeNi(BDC)(F), signifying the absence of the DMF coordination. The coordination of DMF in the Fe-rich FeNi(BDC)(DMF,F) leads to variations in molecular structure and thus the resulting XRD pattern, different from that of the Ni-rich FeNi(BDC)(F), which is without DMF coordination. Fig. 2e and f show the high resolution XPS spectra of Ni2p and Fe2p of FeNi-MOF/NF of Fe:Ni of 5:1 to investigate the oxidation states of Ni and Fe in the MOF. The Fe2p spectrum can be deconvoluted to exhibit constituent binding energy peaks of 724.2 and 710.6 eV for $\text{Fe}2\text{p}_{1/2}$ and $\text{Fe}2\text{p}_{3/2}$, respectively, which suggest an average oxidation state of 3+ for Fe. As for the Ni2p spectrum, the binding energy peaks located at 873.0 and 855.7 eV can be attributed to $\text{Ni}2\text{p}_{1/2}$ and $\text{Ni}2\text{p}_{3/2}$, respectively, whereas the other two peaks located at 879.1 and 861.4 eV are the satellite peaks of $\text{Ni}2\text{p}_{1/2}$ and $\text{Ni}2\text{p}_{3/2}$, respectively, from which one can conclude an average oxidation state of 2+ for Ni.

The reference Fe(BDC)(DMF) MOF possesses Fe ions with an average oxidation state of 2+, which is a direct result of replacing OH with DMF as the coordination group [54]. For the present Fe-rich FeNi(BDC)(DMF,F) MOF, partial substitution of DMF with highly electronegative F^- increases the valence of Fe to maintain the charge balance, thus raising the average oxidation state of Fe to 3+. The preferred affinity of F^- towards Fe than towards other metal atoms in fact has been demonstrated in literature [53,63].

The electrocatalytic performances of MOF/NF electrodes toward the OER and HER were investigated in 1 M KOH electrolyte in a typical three-electrode system, with those of blank NF, bulk MOF/NF, and common benchmark electrode IrO_2/NF for the OER, included for comparison. First, the effect of Ni loading toward the OER was investigated. Figs. 3a, b, S6a, and S6b show the LSV polarization curves of the MOF/NF electrodes fabricated at increasing Ni precursor loading, from 0 to 100%, from which the overpotentials at specific current densities can be determined. Here, Fig. 3a and b show the LSV polarization curves at selected Fe:Ni ratios, whereas Figs. S6a and S6b show

the complete set of the LSV polarization curves. Figs. 3b and S6b show the LSV polarization curves at a locally enlarged potential window from which the detailed characteristics of the polarization curves can be more clearly observed. Several points can be made from Figs. 3b and S6b. First, for the Ni-only MOF/NF electrode, there exists a pronounced oxidation peak, attributable to the oxidation of Ni^{2+} to Ni^{3+} to form the active intermediate responsible for the OER [64]. Following this oxidation peak is the occurrence of the OER, monotonically increasing the current density with increasing applied potential. Second, upon incorporation of Fe into the MOF, the oxidation peak is pushed toward the more positive potential region, whereas the onset of the OER is pushed toward the less positive potential region, leading to overlapping of the two events. With increasing Fe loading in the MOF, the oxidation peak diminishes and the onset of the OER is further pushed toward the less positive region, resulting in smaller overpotentials at specific current densities. If the Fe loading is further increased, the onset of the OER is pushed toward the more positive potential region. Consequently, there exists an optimal Fe loading of the MOF, Fe:Ni of 5:1, to acquire the lowest overpotentials. It is important to note that, when determining the overpotentials for the OER, the possible interference from the oxidation peak has to be avoided. Here, the overpotentials at 60 mA cm^{-2} , η_{60} , were determined instead of the more common η_{10} . The results are summarized in Table S4 (Supporting Information) for comparison. Evidently, all MOF/NF electrodes show better electrocatalytic performances than blank NF ($\eta_{60} = 423\text{ mV}$), and all bimetallic MOF/NF electrodes exhibit lower overpotentials than the two monometallic MOF/NF electrodes ($\eta_{60} = 304$ and 358 mV for Fe-only and Ni-only MOF/NF electrodes, respectively). The bimetallic MOF/NF electrode of Fe:Ni of 5:1 shows the lowest overpotential of 227 mV at 60 mA cm^{-2} , significantly outperforming all other electrodes. It is worth noting that there exists a strong correlation between the composition (and thus morphology and crystalline phase) and the electrocatalytic activities of the bimetallic MOF/NF electrodes. Basically, Fe-rich FeNi(BDC)(DMF,F)/NF electrodes perform better than Ni-rich FeNi(BDC)(F)/NF electrodes.

Furthermore, Tafel slopes and electrochemical impedance spectroscopy (EIS) measurements were investigated to study the electrochemical kinetic characteristics of the electrodes. Tafel slopes, with a unit of mV dec^{-1} , signifies the potential needed to attain a tenfold current density and is determined by recasting the polarization data into Tafel equation. To be a fair comparison, it is essential to determine Tafel slopes within a similar current density window for all electrodes. The results are presented in Figs. 3c and S6c. Evidently, the Fe-rich FeNi(BDC)(DMF,F)/NF electrode of Fe:Ni of 5:1 exhibits the lowest Tafel slope of 37.4 mV dec^{-1} among all tested electrodes. With this low Tafel slope, the Fe-rich FeNi(BDC)(DMF,F)/NF electrode of Fe:Ni of 5:1 achieves an extremely low overpotential of 252 mV at a high current density of 400 mA cm^{-2} , largely outperforming all other tested electrodes. As for the EIS, it was conducted at 1.59 V (vs. RHE) over a frequency range of 100 kHz to 100 mHz in 1 M KOH . The setting of 1.59 V is to ensure the occurrence of the OER for all tested electrodes including blank NF. Figs. 3d and S6d show the resulting Nyquist plots, which are curve-fitted with an equivalent circuit model to extract the critical charge transfer resistance data. The equivalent circuit model is presented as insets of Figs. 3d and S6d, in which R_{ct} , R_s , R_p , CPE, and C_{dl} denote the charge transfer resistance, system resistance, electrode porosity resistance, constant phase element, and double-layer capacitance, respectively. The determined R_{ct} values are summarized in Table S4 for comparison. Fe-rich FeNi(BDC)(DMF,F)/NF electrode of Fe:Ni of 5:1 has the smallest R_{ct} value of $0.143\ \Omega$, significantly smaller than the values of 0.588 , 0.203 , 0.415 , and $0.898\ \Omega$ of the MOF/NF electrodes of nickel precursor loading of 0, 33, 75, and 100%, respectively. The small R_{ct} value indicates the efficient electron transfer between the active sites of the MOF/NF electrode and the electrolyte ions during the OER. Both Tafel slopes and R_{ct} values suggest that bimetallic MOF/NF electrodes exhibit better electrocatalytic performances than monometallic

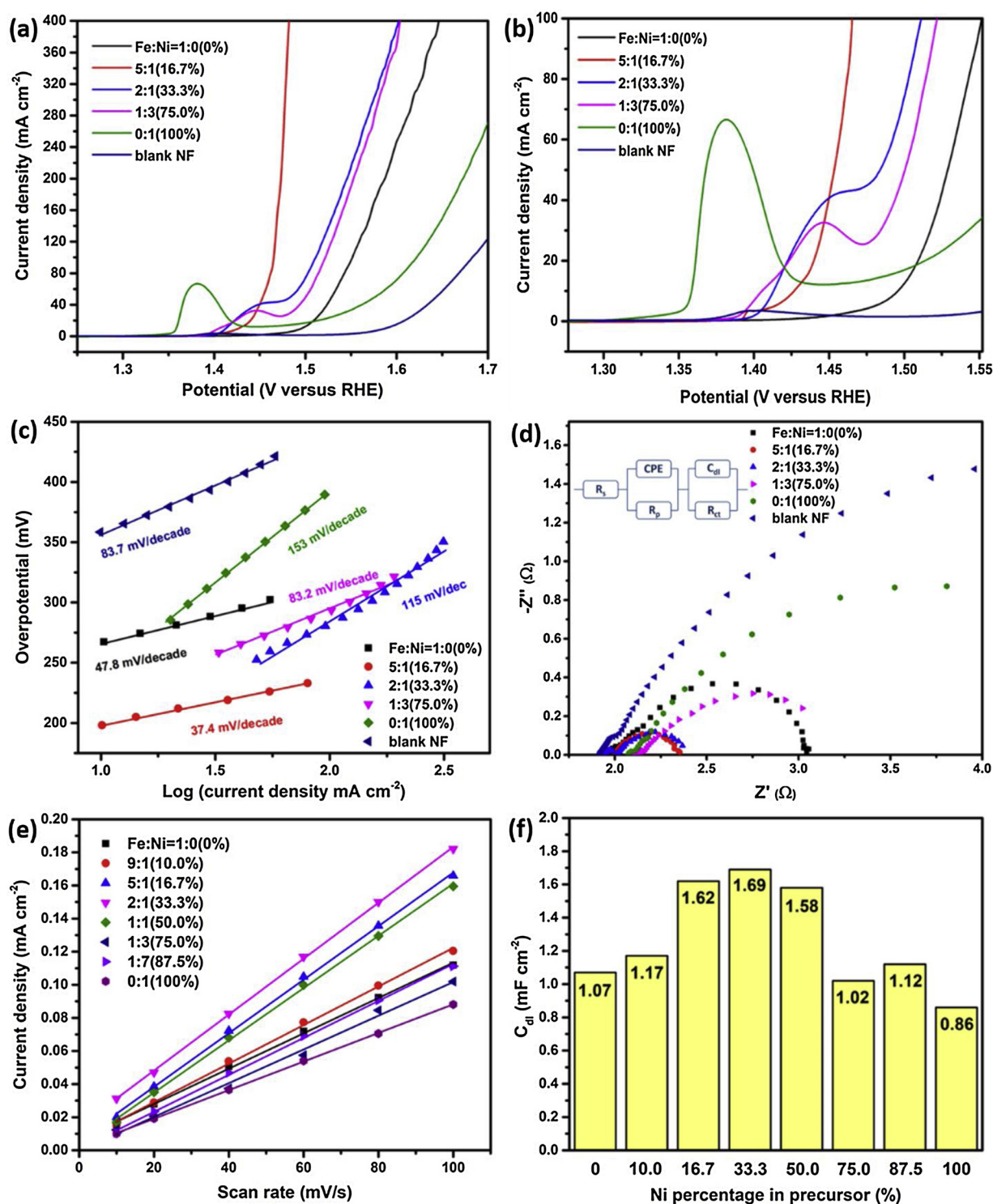


Fig. 3. Comparison of electrocatalytic performances of MOF/NF fabricated at increasing Ni loading toward OER: (a) linear sweep voltammetric polarization curves, (b) linear sweep voltammetric polarization curves at locally enlarged potential window, (c) Tafel slopes, (d) Nyquist plots at 1.59 V (vs. RHE) over frequency range of 100 kHz to 100 mHz in 1 M KOH, (e) capacitive current density vs. scan rate curves for electrochemically active surface area (ECSA) measurements, (f) C_{dl} values of MOF/NF electrodes as function of Ni precursor percentage.

MOF/NF electrodes, because of the positive synergistic effects between the Fe-rich and Ni-rich MOFs, and there exists an optimal bimetallic composition to achieve the strongest synergistic effects for the best electrocatalytic performances toward the OER, in terms of overpotentials at low and high current densities, Tafel slope, and charge transfer resistance. Turnover frequencies (TOF) (Table S4, Supporting Information) for the OER of these MOF/NF electrodes were also

determined to further confirm the point. The key parameter, the number of surface active sites, was estimated from the reductive negative scan peak area [65], and the TOFs were determined at 1.48 V (vs. RHE). The MOF/NF electrode of Fe:Ni of 5:1 shows the highest TOF value of 0.298, again confirming the fundamental advantages of this catalyst.

To gain further insight on the electrocatalytic activities of the MOF/

NF electrodes, measurements of electrochemical surface areas (ECSA), which can be determined from the electrochemical double-layer capacitance (C_{dl}), were conducted. ECSA (or C_{dl}) is a good measure of the quantity of the active sites, which is also good reflection of the morphology and porous structure of the electrode. Basically, cyclic voltammograms (CV) were recorded within a non-Faradaic potential window (0.789–0.939 V vs. RHE) at increasing scan rates (10–100 mV/s) to obtain C_{dl} values. Fig. 3e shows the resulting capacitive current density at 0.864 V (vs. RHE) vs. scan rate curves, from which C_{dl} are determined from the slopes of the fitted lines. Here, the C_{dl} value is directly proportional to ECSA, and thus can be compared as a measure of ECSA. Fig. 3f summarizes the C_{dl} values as a function of the metallic composition of the MOF. Evidently, Fe-rich FeNi(BDC)(DMF,F)/NF electrodes of Fe:Ni of 1:1, 2:1, and 5:1 exhibit comparable C_{dl} , significantly larger than the rest. Interestingly, the C_{dl} value of the electrode of Fe:Ni of 5:1 (1.62) is slightly smaller than that of the electrode of Fe:Ni of 2:1 (1.69). It is to be noted that ECSA alone cannot completely determine the electrocatalytic activity of the electrode since it is only a measure for the quantity of the active sites and the quality of the active sites also matters. The synergistic effects between well mixed Fe-rich and Ni-rich MOFs lead to the highest.

TOF, a good measure for the intrinsic activity of the active sites. It is well accepted that to boost the electrochemical performances of catalysts, one should consider both quantity and quality of the active sites, which may be quantified by ECSA and TOF, respectively [66]. Consequently, the electrode of Fe:Ni of 5:1 with the highest TOF value shows the best catalytic performance, although its C_{dl} is slightly smaller than that of the electrode of Fe:Ni of 2:1.

The best performing FeNi(BDC)(DMF,F)/NF electrode of Fe:Ni of 5:1 was further compared with other comparison electrodes toward the OER, including bulk FeNi(BDC)(DMF,F)/NF of Fe:Ni of 5:1 (bulk FeNi(BDC)(DMF,F) powders coated on NF), benchmark IrO_2 /NF, and blank NF. The results, including LSV polarization curves, Tafel slopes, and Nyquist plots, are presented in Fig. 4 for comparison. The FeNi(BDC)(DMF,F)/NF electrode delivers the current density of 60 mA cm^{-2} at an ultralow overpotential of 227 mV, significantly lower than 301 mV achieved by the bulk FeNi(BDC)(DMF,F)/NF electrode. This outcome suggests that chemical in-situ growth of the MOFs on the support is a much better practice than physical coating of the MOF powders on the support with non-conductive binders, attributable to the much better chemical and electronic contacts between the MOFs and the support achieved through in-situ MOF growth. The bulk FeNi(BDC)(DMF,F)/NF electrode however outperforms the IrO_2 /NF electrode in terms of η_{60} , 301 vs. 370 mV, indicating the superior intrinsic catalytic activity of this bimetallic MOF over IrO_2 . At high current densities, such as 400 mA cm^{-2} , the FeNi(BDC)(DMF,F)/NF electrode outperforms the bulk FeNi(BDC)(DMF,F)/NF and IrO_2 electrodes in terms of η_{400} at even greater extent, 252 vs. 345 mV of the bulk FeNi(BDC)(DMF,F)/NF electrode and 540 mV of the IrO_2 /NF electrode. In terms of overpotentials, the Fe(BDC)(DMF,F)/NF electrode is superior to many recently reported NF-based electrodes, such as NiCo_2S_4 /NF ($\eta_{10} = 260 \text{ mV}$) [67], Co-Ni-B@NF ($\eta_{10} = 313 \text{ mV}$) [68], Co(OH)_2 @NCNTs/NF ($\eta_{10} = 270 \text{ mV}$) [69], S-NiFe₂O₄/NF ($\eta_{10} = 267 \text{ mV}$) [70], Ni-Co-P HNBs on NF ($\eta_{10} = 270 \text{ mV}$) [71], FeCoP UNSAs ($\eta_{20} = 260 \text{ mV}$) [72], Fe/Ni-BTC/NF ($\eta_{10} = 270 \text{ mV}$) [73], NiFe-MOF-74/NF ($\eta_{10} = 223 \text{ mV}$) [74], Fe-MOF array/NF ($\eta_{50} = 240 \text{ mV}$) [75], and Ni-MOF/NF ($\eta_{100} = 320 \text{ mV}$) [76]. For Tafel slopes, the FeNi(BDC)(DMF,F)/NF electrode exhibits an ultralow value of 37.4 mV dec^{-1} , again significantly outperforming the bulk FeNi(BDC)(DMF,F)/NF (58.8 mV dec^{-1}) and IrO_2 /NF (75.6 mV dec^{-1}) electrodes. As for the R_{ct} values extracted from the Nyquist plots, the FeNi(BDC)(DMF,F)/NF electrode stands out among the three comparison electrodes with a small charge transfer resistance of 0.143Ω , significantly smaller than those of the bulk FeNi(BDC)(DMF,F)/NF (0.370Ω) and IrO_2 /NF (0.802Ω) electrodes.

The inter-molecular synergistic effects between the Fe-rich FeNi

(BDC)(DMF,F) and Ni-rich FeNi(BDC)(F) phases and intra-molecular synergistic effects between the FeO_6 and NiO_6 clusters within the bimetallic MOFs, work to boost the electrocatalytic performances of the bimetallic MOFs, not only toward the OER but also toward the HER. Fig. 5 shows the comparison in HER performances of four electrodes, the FeNi(BDC)(DMF,F)/NF electrodes of Fe:Ni of 5:1 and 1:1, Fe-only MOF/NF electrode, and Ni-only MOF/NF electrode. Evident from Fig. 5a, both bimetallic MOF/NF electrodes exhibit lower overpotentials than the Fe-only and Ni-only MOF/NF electrodes. To be consistent with the comparison basis of the OER performances, η_{60} are determined and compared between the four MOF/NF electrodes. The parameter η_{10} is also determined to compare with the HER performances of recently reported state-of-the-art HER electrocatalysts. The FeNi(BDC)(DMF,F)/NF electrode of Fe:Ni of 5:1 achieves overpotentials of 234 mV at 60 mA cm^{-2} and 348 mV at 400 mA cm^{-2} , significantly outperforming the other three electrodes, η_{60} of 274 mV for the FeNi(BDC)(DMF,F)/NF electrode of Fe:Ni of 1:1, η_{60} of 308 mV of the Fe-only MOF/NF electrode, and η_{60} of 284 mV for the Ni-only MOF/NF electrode (Table S5, Supporting Information). In terms of η_{10} , the FeNi(BDC)(DMF,F)/NF electrode of Fe:Ni of 5:1, with a value of 160 mV, compare favorably with many recently reported top notch NF-based HER electrocatalysts, including NiCo_2S_4 /NF ($\eta_{10} = 210 \text{ mV}$) [67], Co-Ni-B@NF ($\eta_{10} = 205 \text{ mV}$) [68], Co(OH)_2 @NCNTs/NF ($\eta_{10} = 170 \text{ mV}$) [69], $\text{Co}_1\text{Mn}_1\text{CH}$ /NF ($\eta_{10} = 180 \text{ mV}$) [77], and FeSe_2 on NF ($\eta_{10} = 178 \text{ mV}$) [78]. Tafel slopes and charge transfer resistances extracted from Nyquist plots were also determined to compare the catalytic kinetic characteristics of the electrodes toward the HER. As expected, the FeNi(BDC)(DMF,F) electrode of Fe:Ni of 5:1 exhibits the lowest Tafel slope (96.2 mV dec^{-1}) among all four MOF/NF electrodes as shown in Fig. 5b. EIS was conducted at -0.310 V (vs. RHE) over a frequency range of 100 kHz to 100 mHz in 1 M KOH to ensure the occurrence of the HER for all tested electrodes. Fig. 5c shows the resulting Nyquist plots of the four MOF/NF electrodes, from which the R_{ct} values are determined and summarized in Table S5 (Supporting Information) for comparison. The FeNi(BDC)(DMF,F) electrode of Fe:Ni of 5:1 again exhibits the lowest R_{ct} value of 0.799Ω , consistent with its highest electrocatalytic activity among the four MOF/NF electrodes.

Because of its outstanding OER and HER performances, the FeNi(BDC)(DMF,F)/NF electrode of Fe:Ni of 5:1 was further applied as a bifunctional electrocatalyst for overall water splitting. The overall water splitting was conducted in a two-electrode system in 1 M KOH. In addition to the FeNi(BDC)(DMF,F)/NF//FeNi(BDC)(DMF,F)/NF couple of Fe:Ni of 5:1, the benchmark couple Pt-C/NF// IrO_2 /NF, bulk FeNi(BDC)(DMF,F)/NF//bulk FeNi(BDC)(DMF,F)/NF couple of Fe:Ni of 5:1, and blank NF//blank NF couple were also tested for comparison. It requires only 1.58 V for the FeNi(BDC)(DMF,F)/NF//FeNi(BDC)(DMF,F)/NF couple to reach a current density of 10 mA cm^{-2} (Fig. 6a), lower than those of the bulk FeNi(BDC)(DMF,F)/NF//bulk FeNi(BDC)(DMF,F)/NF couple (1.64 V), Pt-C/NF// IrO_2 /NF couple (1.67 V), and blank NF//blank NF couple (1.80 V). As for Tafel slopes, the FeNi(BDC)(DMF,F)/NF//FeNi(BDC)(DMF,F)/NF couple shows a low value of 159 mV dec^{-1} , comparable with that of the Pt-C/NF// IrO_2 /NF couple (160 mV dec^{-1}). A complete comparison of FeNi(BDC)(DMF,F)/NF as a bifunctional electrocatalyst against recently reported state-of-the-art bifunctional NF based electrocatalysts concerning OER, HER, full cell, and stability test performances, is presented in Table S6 (Supporting Information) [67,69,72,79–82].

Possible reasons for the observed improvements in electrocatalytic performances effected by the inter-molecular and intra-molecular synergistic effects of the adequately modulated bimetallic FeNi-MOF, are discussed below. Although the fundamental mechanism of the synergistic effects remains debatable, some speculations are proposed below according to relevant findings reported in recent literature [83–87]. It has been proved that the presence of Fe affects the redox characteristics of Ni, causing positive potential shifts accompanied with intensity suppression resulting from the decrease of the average

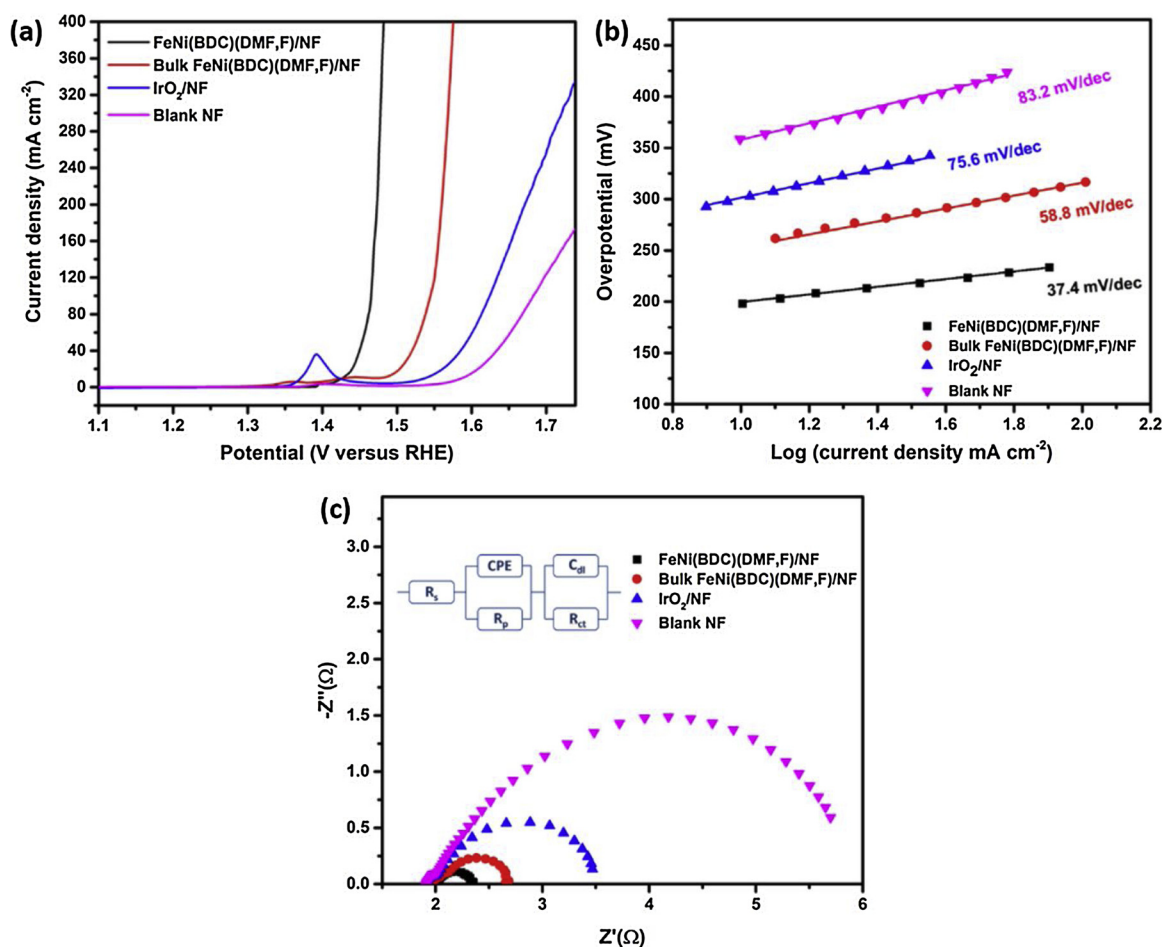


Fig. 4. Comparison in OER performances: (a) LSV polarization curves, (b) Tafel slopes, and (c) Nyquist plots at 1.59 V (vs. RHE) over frequency range of 100 kHz to 100 mHz in 1 M KOH for FeNi(BDC)(DMF,F)/NF of Fe:Ni of 5:1, bulk FeNi(BDC)(DMF,F)/NF of Fe:Ni of 5:1, IrO₂/NF, and blank NF electrodes.

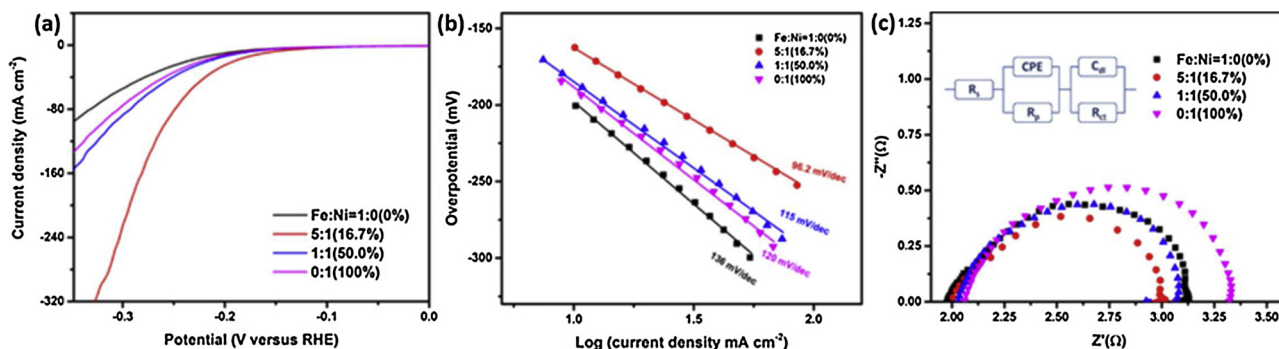


Fig. 5. Comparison in HER performances: (a) LSV polarization curves, (b) Tafel slopes, and (c) Nyquist plots at -0.310 V (vs. RHE) over frequency range of 100 kHz to 100 mHz in 1 M KOH for FeNi(BDC)(DMF,F)/NF electrodes of Fe:Ni of 1:0, 5:1, 1:1, and 0:1.

oxidation state of the Ni sites. This phenomenon implies changes in local electronic environment of Ni–O, and the result is to increase the electrocatalytic activity toward the OER, revealed as the synergistic effect. The increase in electrocatalytic activity however is achieved at the expense of decrease in active site numbers, leading to existence of an optimal metallic composition for the highest synergistic effect [83,85]. From a different point of view, DFT simulations show that the incorporated Fe cations are the more active sites in FeNi bimetallic systems [64]. The increase in Fe incorporation however leads to formation of inactive γ -FeOOH phase [84]. Consequently, competition of the two opposite effects results in the existence of an optimal metallic composition to achieve the strongest synergistic effect. Despite the

differences existing in the detailed synergistic mechanism, both proposals stress on the alteration of the electronic environment of the metal sites and emergence of opposite competing effects [87].

Here, the redox characteristics of the present MOF materials, including Fe-only, bimetallic, and Ni-only MOFs, were studied with cyclic voltammetry to gain further insight on the synergistic effects. The bulk MOF powders were coated on graphite electrodes, instead of nickel foam, for the CV study to avoid the interferences coming from nickel foam. The results are presented in Fig. S8 (Supporting Information), and it is evident that the redox couples of the MOFs shift to the more positive potential region with increasing Fe incorporation, accompanied by decrease in peak intensity. The oxidation peak in fact overlaps with

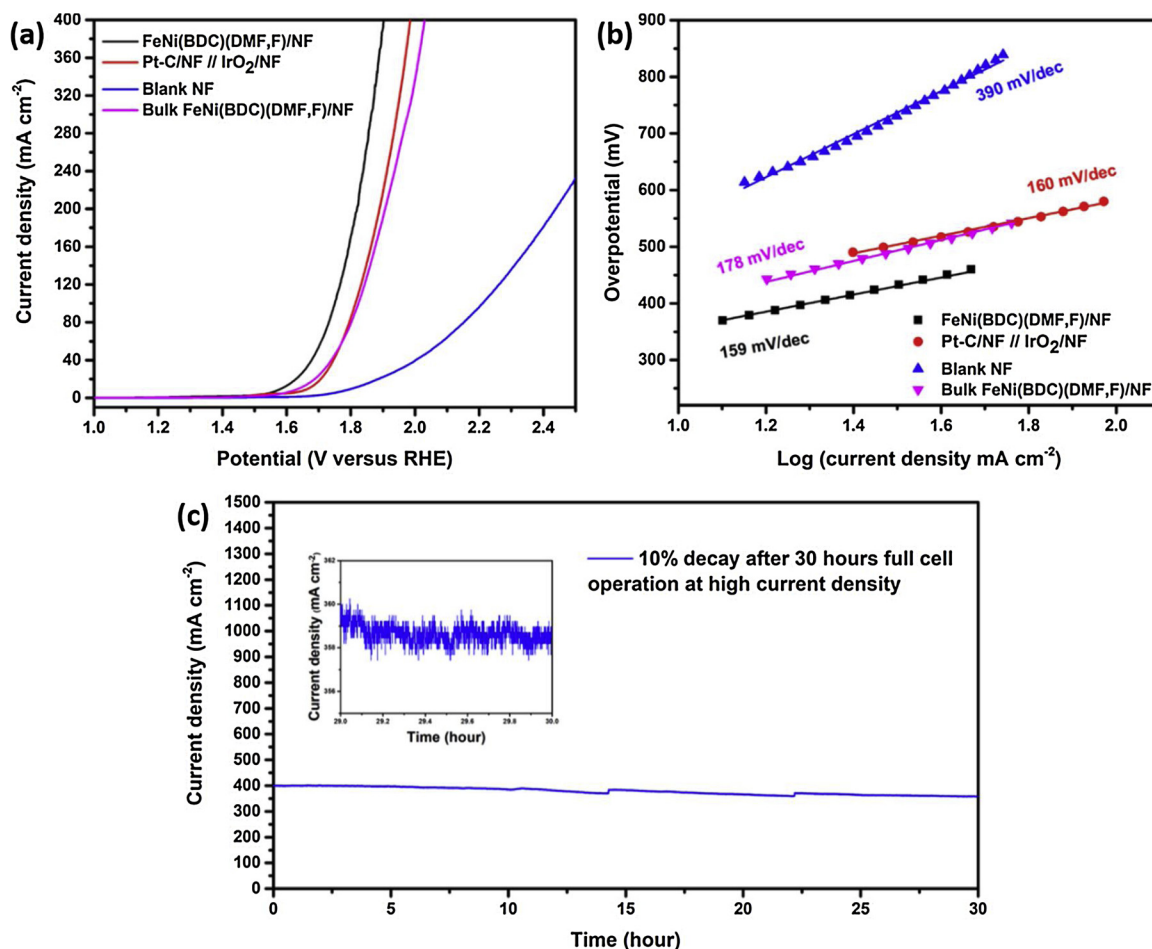


Fig. 6. Comparison in overall water splitting performances: (a) LSV polarization curves and (b) Tafel slopes for FeNi(BDC)(DMF,F)/NF//FeNi(BDC)(DMF,F)/NF couple of Fe:Ni of 5:1, bulk FeNi(BDC)(DMF,F)/NF//bulk FeNi(BDC)(DMF,F)/NF couple of Fe:Ni of 5:1, Pt-C/NF//IrO₂/NF couple, and blank NF//blank NF couple. (c) Chronoamperometric (i-t) full cell stability test of FeNi(BDC)(DMF,F)/NF//FeNi(BDC)(DMF,F)/NF couple of Fe:Ni of 5:1 at 400 mA cm⁻² for 30 h. Bumps of current density curve were caused by addition of water to maintain liquid level and concentration of electrolyte. Inset shows fluctuation in current density resulting from violent bubble generation.

the OER curve, appearing as a shoulder of the OER curve, and diminishes in intensity, eventually fading out with increasing Fe incorporation. This phenomenon implies that the average oxidation state of Ni decreases and the oxidation of Ni is suppressed with increasing Fe incorporation, consistent with the finding reported in literature [83]. The decrease in average oxidation state of Ni can be further confirmed with high resolution XPS spectra of Ni2p of the Ni-only MOF/NF electrode (Fig. S9, Supporting Information). The Ni2p spectra is deconvoluted to exhibit peaks with binding energies of 873.7 and 856.4 eV for Ni2p_{1/2} and Ni2p_{3/2}, respectively. For comparison, the FeNi(BDC)(DMF,F)/NF electrode of Fe:Ni of 5:1 exhibits binding energies of 873.0 and 855.7 eV for Ni2p_{1/2} and Ni2p_{3/2}, respectively, showing a binding energy down shift of 0.7 eV. This down shift in binding energy suggests decrease in the average oxidation state of Ni in bimetallic FeNi-MOF as compared with that in Ni-only MOF, confirming the change of the electronic environment of the metal sites induced through alloying. Based on the above experimental data and findings from literature, it can be proposed that the inter-molecular and intra-molecular synergistic effects are derived from the competition between the increasing activity of the metal sites induced from alloying single metallic MOFs and the decreasing number of the more active metal sites available in the bimetallic MOF. This competition characteristic also ensures the existence of an optimal composition of the constituent metallic species. In other words, bimetallic MOFs can be adequately modulated in metal composition to achieve the highest electrocatalytic

activities.

In addition to electrocatalytic performances, the long-term stability of the electrode when operated at high current densities is also essential for practical applications. The stability of the FeNi(BDC)(DMF,F)/NF//FeNi(BDC)(DMF,F)/NF couple was tested at a high current density of 400 mA cm⁻² with chronoamperometric measurements for overall water splitting for 30 h. The FeNi(BDC)(DMF,F)/NF//FeNi(BDC)(DMF,F)/NF couple experienced only 10% decay in current density. It has to be noted that during a long-term stability test at high current densities, intensive electrochemical reactions occur and large amounts of H₂ and O₂ bubbles are generated on the electrodes, placing a great deal of electrochemical and mechanical stresses on the electrocatalysts, thus deteriorating the electrodes electrochemically and mechanically. The excellent durability of the electrodes can be further confirmed with SEM, HRXPS, and LSV before and after the stability test. As shown in Fig. S10 (Supporting Information), the morphology of the electrode after the test is similar to that of the electrode before the test as presented in Fig. 1c. Fig. S11 (Supporting Information) shows the full survey XPS spectra of the electrode before and after the test and the high-resolution XPS spectra of Fe2p and Ni2p after the test. The two full survey XPS spectra are similar to each other, except for a K2p peak appearing in the after test spectrum, which is contributed by the residual electrolyte, KOH. As to the spectra for Fe2p and Ni2p, close comparison between Figs. 2e and S11b and 2f and S11a reveals that the corresponding spectra remain similar after the test. The LSV

polarization curves recorded before and after the OER test (Fig. S12a, Supporting Information) and after the HER test (Fig. S12b, Supporting Information) are in good agreement with each other. Furthermore, we determined the concentrations of Fe and Ni in the electrolyte with an inductively coupled plasma-optical emission spectrometer (ICP-OES) after the test to see how much Fe and Ni have been leached out from the electrode to make further judgement on the stability of the electrode. The concentrations of Fe and Ni in the electrolyte were only 87 and 63 ppb, respectively, which are negligibly small. In conclusion, based on the chronoamperometry, SEM, XPS, LSV, and leaching measurements, the stability of the electrode is excellent. Furthermore, the amounts of the hydrogen and oxygen produced from the overall water splitting, taking the FeNi(BDC)(DMF,F)/NF electrodes as both cathode and anode, operated at 70 mA cm^{-2} for 30 min, were quantified through gas chromatography measurements. It is evident from Fig. S13 (Supporting Information) that the agreement between the experimental and theoretical amounts is excellent, suggesting close to 100% Faradaic efficiencies and absence of gas crossover and side reactions. In addition, the ratio of hydrogen versus oxygen production agrees well with the theoretical value of 2. Finally, we demonstrated the power-to-gas (P2G) and gas-to-power (G2P) approach with a movie, Movie 1, in the SI. In the movie, the present electrolysis cell, FeNi(BDC)(DMF,F)/NF//FeNi(BDC)(DMF,F)/NF, was driven with a solar cell and the produced hydrogen was fed into a fuel cell to generate electricity to drive an electric fan.

4. Conclusion

Highly efficient and stable bifunctional bimetallic metal MOFs based electrocatalysts for overall water splitting at high current densities, were developed through adequately modulating the composition of the two constituent metallic components. The adequately modulated bi-metallic MOF, FeNi(BDC)(DMF,F), composed of two well mixed phases of Fe-rich FeNi(BDC)(DMF,F) and Ni-rich FeNi(BDC)(F), was in-situ grown into conductive, macroporous nickel foam to realize unique hierarchical synergistic effects to achieve outstanding electrocatalytic performances toward overall water splitting at high current densities. The hierarchical synergistic effects involve the MOF/substrate synergistic effects between the FeNi(BDC)(DMF,F) and the conductive nickel foam, the inter-molecular synergistic effects between the two constituent MOF phases, and the intra-molecular synergistic effects between the FeO₆ and NiO₆ clusters of the Fe-rich FeNi(BDC)(DMF,F). The FeNi(BDC)(DMF,F)/NF//FeNi(BDC)(DMF,F)/NF couple delivered current densities of 10 and 400 mA cm^{-2} at ultralow cell voltages of 1.58 and 1.90 V, respectively, with excellent stability, outperforming the pairing of benchmark electrodes, Pt-C/NF//IrO₂/NF. Implementation of the novel hierarchical synergistic effect concept proves to be an effective way to develop ultrahigh performance electrocatalysts.

Declaration of Competing Interest

The authors declare that they have no known competing financial interests or personal relationships that could have appeared to influence the work reported in this paper.

Acknowledgement

The authors acknowledge the financial support offered by the Ministry of Science and Technology of Taiwan, ROC under grant MOST 106-2221-E-007-090-MY2.

Note and references

Appendix A. Supplementary data

Supplementary material related to this article can be found, in the

online version, at doi:<https://doi.org/10.1016/j.apcatb.2019.118023>.

References

- [1] B.Y. Guan, X.Y. Yu, H.B. Wu, X.W. Lou, *Adv. Mater.* 29 (2017) 1703614.
- [2] M.R. Lukatskaya, S. Kota, Z.F. Lin, M.Q. Zhao, N. Shpigel, M.D. Levi, J. Halim, P.L. Taberna, M. Barsoum, P. Simon, Y. Gogotsi, *Nat. Energy* 2 (2017) 17105.
- [3] I. Roger, M.A. Shipman, M.D. Symes, *Nat. Rev. Chem.* 1 (2017) 0003.
- [4] R. Eisenberg, *Science* 324 (2009) 44–45.
- [5] D.R. Dekel, *J. Power Sources* 375 (2018) 158–169.
- [6] F.S. da Silva, T.M. de Souza, *Int. J. Hydrogen Energy* 42 (2017) 26020–26036.
- [7] N.T. Suen, S.F. Hung, Q. Quan, N. Zhang, Y.J. Xu, H.M. Chen, *Chem. Soc. Rev.* 46 (2017) 337–365.
- [8] B. You, N. Jiang, X. Liu, Y.J. Sun, *Angew. Chem.-Int. Ed.* 55 (2016) 9913–9917.
- [9] K. Zeng, D.K. Zhang, *Prog. Energy Combust. Sci.* 36 (2010) 307–326.
- [10] T. Audichon, T.W. Napporn, C. Canaff, C. Morais, C. Comminges, K.B. Kokoh, *J. Phys. Chem. C* 120 (2016) 2562–2573.
- [11] Y.P. Zhu, T.Y. Ma, M. Jaroniec, S.Z. Qiao, *Angew. Chem.-Int. Ed.* 56 (2017) 1324–1328.
- [12] P. Li, R. Zhao, H. Chen, H. Wang, P. Wei, H. Huang, Q. Liu, T. Li, X. Shi, Y. Zhang, *Small* 15 (2019) 1805103.
- [13] X.Y. Yu, Y. Feng, B.Y. Guan, X.W. Lou, U. Paik, *Energy Environ. Sci.* 9 (2016) 1246–1250.
- [14] Y.H. Cheng, J.N. Guo, Y. Huang, Z.J. Liao, Z.H. Xiang, *Nano Energy* 35 (2017) 115–120.
- [15] C.J. Xuan, J. Wang, W.W. Xia, Z.K. Peng, Z.X. Wu, W. Lei, K.D. Xia, H.L.L. Xin, D.L. Wang, *ACS Appl. Mater. Interfaces* 9 (2017) 26134–26142.
- [16] T. Liu, L. Xie, J. Yang, R. Kong, G. Du, A.M. Asiri, X. Sun, L. Chen, *ChemElectroChem* 4 (2017) 1840–1845.
- [17] X. Ji, R. Zhang, X. Shi, A.M. Asiri, B. Zheng, X. Sun, *Nanoscale* 10 (2018) 7941–7945.
- [18] Z. Niu, C. Qiu, J. Jiang, L. Ai, *ACS Sustain. Chem. Eng.* 7 (2018) 2335–2342.
- [19] F. Song, K. Schenk, X.L. Hu, *Energy Environ. Sci.* 9 (2016) 473–477.
- [20] Y. Liu, N. Han, J. Jiang, L. Ai, *Int. J. Hydrogen Energy* 44 (2019) 10627–10636.
- [21] C. Qiu, L. Ai, J. Jiang, *ACS Sustain. Chem. Eng.* 6 (2018) 4492–4498.
- [22] C. Tang, N.Y. Cheng, Z.H. Pu, W. Xing, X.P. Sun, *Angew. Chem.-Int. Ed.* 54 (2015) 9351–9355.
- [23] J.W. Nai, Y. Lu, L. Yu, X. Wang, X.W. Lou, *Adv. Mater.* 29 (2017) 1703870.
- [24] Z. Wang, X. Ren, L. Wang, G. Cui, H. Wang, X. Sun, *ChCom* 54 (2018) 10993–10996.
- [25] H.N. Ren, Z.H. Huang, Z.Y. Yang, S.J. Tang, F.Y. Kang, R.T. Lv, J. Energy Chem. 26 (2017) 1217–1222.
- [26] Q. Liu, L. Xie, Z. Liu, G. Du, A.M. Asiri, X. Sun, *ChCom* 53 (2017) 12446–12449.
- [27] C. Chang, L. Zhang, C.W. Hsu, X.F. Chuah, S.Y. Lu, *ACS Appl. Mater. Interfaces* 10 (2018) 417–426.
- [28] L. Zhang, C. Chang, C.W. Hsu, C.W. Chang, S.Y. Lu, *J. Mater. Chem. A* 5 (2017) 19656–19663.
- [29] L. Zhang, J.S. Hu, X.H. Huang, J. Song, S.Y. Lu, *Nano Energy* 48 (2018) 489–499.
- [30] X.-F. Chuah, C.-T. Hsieh, C.-L. Huang, D. Senthil Raja, H.-W. Lin, S.-Y. Lu, *ACS Appl. Energy Mater.* 2 (2018) 743–753.
- [31] C.T. Hsieh, X.F. Chuah, C.L. Huang, H.W. Lin, Y.A. Chen, S.Y. Lu, *Small Methods* (2019), <https://doi.org/10.1002/smt.201900234> in press.
- [32] C.-L. Huang, X.-F. Chuah, C.-T. Hsieh, S.-Y. Lu, *ACS Appl. Mater. Interfaces* 1 (2019) 24096–24106.
- [33] S.E. Miller, M.H. Teplensky, P.Z. Moghadam, D. Fairen-Jimenez, *Interface Focus* 6 (2016) 20160027.
- [34] W. Liu, X.B. Yin, *Trac-Trends Anal. Chem.* 75 (2016) 86–96.
- [35] S.H. Kazemi, B. Hosseinzadeh, H. Kazemi, M.A. Kiani, S. Hajati, *ACS Appl. Mater. Interfaces* 10 (2018) 23063–23073.
- [36] Z.Y. Wei, W.X. Zhu, Y.G. Li, Y.Y. Ma, J. Wang, N. Hu, Y.R. Suo, J.L. Wang, *Inorg. Chem.* 57 (2018) 8422–8428.
- [37] T. Tian, Z.X. Zeng, D. Vulpe, M.E. Casco, G. Divitini, P.A. Midgley, J. Silvestre-Albero, J.C. Tan, P.Z. Moghadam, D. Fairen-Jimenez, *Nat. Mater.* 17 (2018) 174–179.
- [38] S. Yuan, L. Feng, K. Wang, J. Pang, M. Bosch, C. Lollar, Y. Sun, J. Qin, X. Yang, P. Zhang, *Adv. Mater.* (2018) 1704303.
- [39] N. Stock, S. Biswas, *Chem. Rev.* 112 (2011) 933–969.
- [40] Y.K. Hwang, D.Y. Hong, J.S. Chang, S.H. Jung, Y.K. Seo, J. Kim, A. Vimont, M. Daturi, C. Serre, G. Ferey, *Angew. Chem.-Int. Ed.* 47 (2008) 4144–4148.
- [41] H. Zhang, J. Nai, L. Yu, X.W.D. Lou, *Joule* 1 (2017) 77–107.
- [42] L.H. Ai, T. Tian, J. Jiang, *ACS Sustain. Chem. Eng.* 5 (2017) 4771–4777.
- [43] Y. Xu, W.G. Tu, B.W. Zhang, S.M. Yin, Y.Z. Huang, M. Kraft, R. Xu, *Adv. Mater.* 29 (2017) 1605957.
- [44] J.J. Duan, S. Chen, C. Zhao, *Nat. Commun.* 8 (2017) 15341.
- [45] D.S. Raja, H.-W. Lin, S.-Y. Lu, *Nano Energy* 57 (2019) 1–13.
- [46] D.S. Raja, X.F. Chuah, S.Y. Lu, *Adv. Energy Mater.* 8 (2018) 1801065.
- [47] M. Gong, H. Dai, *Nano Res.* 8 (2015) 23–39.
- [48] Z.P. Zhang, Y.S. Qin, M.L. Dou, J. Ji, F. Wang, *Nano Energy* 30 (2016) 426–433.
- [49] C. Andronescu, S. Barwe, E. Ventosa, J. Masa, E. Vasile, B. Konkena, S. Moller, W. Schuhmann, *Angew. Chem.-Int. Ed.* 56 (2017) 11258–11262.
- [50] J. Liang, Y.Z. Wang, C.C. Wang, S.Y. Lu, *J. Mater. Chem. A* 4 (2016) 9797–9806.
- [51] B.A. Lu, D.X. Cao, P. Wang, G.L. Wang, Y.Y. Gao, *Int. J. Hydrogen Energy* 36 (2011) 72–78.
- [52] N.K. Chaudhari, H. Jin, B. Kim, K. Lee, *Nanoscale* 9 (2017) 12231–12247.
- [53] Q. Sun, M. Liu, K. Li, Y. Han, Y. Zuo, F. Chai, C. Song, G. Zhang, X. Guo, *Inorg.*

- Chem. Front. 4 (2017) 144–153.
- [54] T.R. Whitfield, X.Q. Wang, L.M. Liu, A.J. Jacobson, Solid State Sci. 7 (2005) 1096–1103.
- [55] A. Mesbah, P. Rabu, R. Sibille, S. Lebègue, T. Mazet, B. Malaman, M. François, Inorg. Chem. 53 (2014) 872–881.
- [56] A. Shastri, A.K. Das, S. Krishnakumar, P.J. Singh, B. Raja Sekhar, J. Chem. Phys. 147 (2017) 224305.
- [57] T. Jao, I. Scott, D. Steele, J. Mol. Spectrosc. 92 (1982) 1–17.
- [58] C.M. Ståkhandske, J. Mink, M. Sandström, I. Pápai, P. Johansson, Vib. Spectrosc. 14 (1997) 207–227.
- [59] L. Ai, C. Zhang, L. Li, J. Jiang, Appl. Catal. B 148 (2014) 191–200.
- [60] J. Gordon, H. Kazemian, S. Rohani, Microporous Mesoporous Mater. 162 (2012) 36–43.
- [61] F. Davar, Z. Fereshteh, M. Salavati-Niasari, J. Alloys. Compd. 476 (2009) 797–801.
- [62] J.A. Simon, P. Vickraman, B.J. Reddy, J. Electroanal. Chem. 823 (2018) 342–349.
- [63] M.I. Breeze, G. Clet, B.C. Campo, A. Vimont, M. Daturi, J.-M. Grenèche, A.J. Dent, F. Millange, R.I. Walton, Inorg. Chem. 52 (2013) 8171–8182.
- [64] J. Liang, Y.-Z. Wang, C.-C. Wang, S.-Y. Lu, J. Mater. Chem. A 4 (2016) 9797–9806.
- [65] S. Anantharaj, S. Ede, K. Karthick, S.S. Sankar, K. Sangeetha, P. Karthik, S. Kundu, Energy Environ. Sci. 11 (2018) 744–771.
- [66] Z.W. Seh, J. Kibsgaard, C.F. Dickens, I. Chorkendorff, J.K. Nørskov, T.F. Jaramillo, Science 355 (2017) eaad4998.
- [67] A. Sivanantham, P. Ganesan, S. Shanmugam, Adv. Funct. Mater. 26 (2016) 4661–4672.
- [68] N. Xu, G. Cao, Z. Chen, Q. Kang, H. Dai, P. Wang, J. Mater. Chem. A 5 (2017) 12379–12384.
- [69] P. Guo, J. Wu, X.B. Li, J. Luo, W.M. Lau, H. Liu, X.L. Sun, L.M. Liu, Nano Energy 47 (2018) 96–104.
- [70] J.L. Liu, D.D. Zhu, T. Ling, A. Vasileff, S.Z. Qiao, Nano Energy 40 (2017) 264–273.
- [71] E.L. Hu, Y.F. Peng, J.W. Nai, D. Zhao, Y. Hu, X.W. Lou, Energy Environ. Sci. 11 (2018) 872–880.
- [72] L. Zhou, M.G. Shao, J.B. Li, S. Jiang, M. Wei, X. Duan, Nano Energy 41 (2017) 583–590.
- [73] L. Wang, Y. Wu, R. Cao, L. Ren, M. Chen, X. Feng, J. Zhou, B. Wang, ACS Appl. Mater. Interfaces 8 (2016) 16736–16743.
- [74] J. Xing, K. Guo, Z. Zou, M. Cai, J. Du, C. Xu, Chem. Commun. 54 (2018) 7046–7049.
- [75] X. Zhang, Q. Liu, X. Shi, A.M. Asiri, X. Sun, Inorg. Chem. Front. 5 (2018) 1405–1408.
- [76] Q. Liu, L. Xie, X. Shi, G. Du, A.M. Asiri, Y. Luo, X. Sun, Inorg. Chem. Front. 5 (2018) 1570–1574.
- [77] T. Tang, W.-J. Jiang, S. Niu, N. Liu, H. Luo, Y.-Y. Chen, S.-F. Jin, F. Gao, L.-J. Wan, J.-S. Hu, J. Am. Chem. Soc. 139 (2017) 8320–8328.
- [78] T. Ahnfeldt, D. Gunzelmann, T. Loiseau, D. Hirsemann, J. Senker, G. Ferey, N. Stock, Inorg. Chem. 48 (2009) 3057–3064.
- [79] C. Panda, P.W. Menezes, C. Walter, S.L. Yao, M.E. Miehl, V. Gutkin, K. Meyer, M. Driess, Angew. Chem.-Int. Ed. 56 (2017) 10506–10510.
- [80] H. Shi, H. Liang, F. Ming, Z. Wang, Angew. Chem. 129 (2017) 588–592.
- [81] Y.J. Li, H.C. Zhang, M. Jiang, Q. Zhang, P.L. He, X.M. Sun, Adv. Funct. Mater. 27 (2017) 1702513.
- [82] T. Tang, W.-J. Jiang, S. Niu, N. Liu, H. Luo, Y.-Y. Chen, S.-F. Jin, F. Gao, L.-J. Wan, J.-S. Hu, J. Am. Chem. Soc. 139 (2017) 8320–8328.
- [83] M.W. Louie, A.T. Bell, J. Am. Chem. Soc. 135 (2013) 12329–12337.
- [84] D. Friebe, M.W. Louie, M. Bajdich, K.E. Sanwald, Y. Cai, A.M. Wise, M.J. Cheng, D. Sokaras, T.C. Weng, R. Alonso-Mori, R.C. Davis, J.R. Bargar, J.K. Nørskov, A. Nilsson, A.T. Bell, J. Am. Chem. Soc. 137 (2015) 1305–1313.
- [85] J. Xu, J. Li, D. Xiong, B. Zhang, Y. Liu, K.-H. Wu, I. Amorim, W. Li, L. Liu, Chem. Sci. 9 (2018) 3470–3476.
- [86] L. Trotochaud, S.L. Young, J.K. Ranney, S.W. Boettcher, J. Am. Chem. Soc. 136 (2014) 6744–6753.
- [87] R. Subbaraman, D. Tripkovic, K.-C. Chang, D. Strmcnik, A.P. Paulikas, P. Hirunsit, M. Chan, J. Greeley, V. Stamenkovic, N.M. Markovic, Nat. Mater. 11 (2012) 550.